Solar Phys (2015) 290:1963–1980
DOI 10.1007/s11207-015-0735-7

Quiescent and Eruptive Prominences at Solar Minimum: A Statistical Study via an Automated Tracking System

I.P. Loboda[1] · **S.A. Bogachev**[1]

Received: 30 October 2014 / Accepted: 29 June 2015 / Published online: 24 July 2015

Abstract We employ an automated detection algorithm to perform a global study of solar prominence characteristics. We process four months of TESIS observations in the He II 304 Å line taken close to the solar minimum of 2008 – 2009 and mainly focus on quiescent and quiescent-eruptive prominences. We detect a total of 389 individual features ranging from 25×25 to 150×500 Mm^2 in size and obtain distributions of many of their spatial characteristics, such as latitudinal position, height, size, and shape. To study their dynamics, we classify prominences as either stable or eruptive and calculate their average centroid velocities, which are found to rarely exceed 3 km s^{-1}. In addition, we give rough estimates of mass and gravitational energy for every detected prominence and use these values to estimate the total mass and gravitational energy of all simultaneously existing prominences ($10^{12} – 10^{14}$ kg and $10^{29} – 10^{31}$ erg). Finally, we investigate the form of the gravitational energy spectrum of prominences and derive it to be a power-law of index -1.1 ± 0.2.

Keywords Prominences, quiescent · Prominences, dynamics · Prominences, formation and evolution

1. Introduction

Prominences are one of the most noticeable features of the Sun, which, although observed for over a century, are still far from being completely understood. For historical reasons, a distinction is made between prominences that are observed off-limb as luminous formations, and filaments, which are usually seen in absorption on the disk. Physically, these are the same structures consisting of plasma with properties similar to those of the chromosphere, being nearly 100 times denser and cooler than the surrounding corona (Hirayama, 1985; Tandberg-Hanssen, 1995; Labrosse *et al.*, 2010). Prominences vary largely in size, morphology, dynamics, magnetic structure, and the way they are related to the rest of the solar activity. As more of these differences were revealed, new classification schemes were

✉ I.P. Loboda
loboda@sci.lebedev.ru

[1] P.N. Lebedev Physical Institute of the Russian Academy of Sciences, Moscow, Russia

introduced by a number of authors (Pettit, 1932; Severny and Khokhlova, 1953; Zirin, 1966; Leroy, Bommier, and Sahal-Brechot, 1984). In this article, we follow the most general one, which divides prominences into two major classes depending on whether they are part of an active region (active prominences), or whether they exist separately over the quiet Sun (quiescent ones). It is known that instabilities in the magnetic structure supporting both these types of prominences can result in an eruption of some part of their material high into the corona (van Ballegooijen and Martens, 1989; Zhang, 2013). In this case, we additionally classify the prominences as eruptive.

Comparative studies have shown that more than 70 % of prominence eruptions are followed by coronal mass ejections, or CMEs (Gilbert *et al.*, 2000; Gopalswamy *et al.*, 2003; Filippov and Koutchmy, 2008). They, in turn, travel over vast distances from the Sun and have a considerable impact on the heliosphere in general, including the Earth's magnetosphere. At the same time, the exact connection between prominence eruptions and CMEs, as well as the mechanisms of formation and eruption of prominences themselves, are still poorly understood. Existing models of prominence formation consider a number of possible magnetic topologies and mechanisms that can fill them with plasma, while observational data are not sufficient to distinguish between these models (Galsgaard and Longbottom, 1999; Mackay *et al.*, 2010). Similarly, theories of prominence eruptions developed so far suffer from poorly constrained pre-eruptive conditions of the magnetic field and plasma (Lin, Soon, and Baliunas, 2003). In this context, statistical studies of prominences seem particularly useful to provide the necessary parameters and constraints to theories and establish reliable correlations of prominence evolution with other manifestations of solar activity.

For decades, prominences have been observed from Earth in a number of spectral lines, primarily Hα, as well as in radio emission (Labrosse and Gouttebroze, 2001; Heinzel, 2007). A comprehensive study of these phenomena, however, became only possible with the advent of space-based observations. Today, prominences can be observed from space by a number of instruments and in a much wider spectral range. Above all, these observations are free of day–night interruptions and unfavourable atmospheric effects. Most of them are performed in the EUV spectral range, where prominences are best seen in the He II 304 Å line. Despite the vast amounts of data produced by these instruments, most current studies of prominences limit themselves to only examining individual, and usually, the largest events. In this way, however, one risks missing smaller prominences, which are still of great interest, and obtaining an incomplete picture of these phenomena. Therefore, to make use of all the data available, and to study the entire set of prominences, special detection and tracking algorithms need to be applied.

A continuous set of observations produced by the *Extreme ultraviolet Imaging Telescope* (EIT) of the *Solar and Heliospheric Observatory* (SOHO), the *Extreme UltraViolet Imager* (EUVI) of the *Solar TErrestrial RElations Observatory* (STEREO), and the *Atmospheric Imaging Assembly* (AIA) of the *Solar Dynamics Observatory* (SDO) since 1996 now covers a vast period of almost two solar cycles. Nevertheless, only a few attempts have been made so far to use these data for large statistical studies of prominences. Two algorithms have been developed for EIT data (Foullon and Verwichte, 2006; Labrosse, Dalla, and Marshall, 2010) and another one for STEREO-A and -B observations (Wang *et al.*, 2010). Furthermore, only the latter attempt produced a prominence catalogue that is now publicly available online. Continuing this line of study, we have developed a new algorithm capable of precisely locating prominences using monochromatic observations in the He II 304 Å line only. We employ this algorithm to study a period of four months of observations, which roughly corresponds to the end of the prolonged solar minimum of 2008 – 2009. Hence, we mainly focus on quiescent and quiescent-eruptive prominences and leave active prominences for future studies.

The organization of this paper is as follows: in Section 2 we present the observational data used and in Section 3 we give a general description of the detection algorithm employed. We then review the major results of its operation and perform a statistical analysis of the obtained prominence parameters in Section 4. Finally, we discuss the system's performance, as well as advantages and future prospects of automated detection of prominences in Section 5.

2. Observations

For this study, we used observations from one of the two *Full-disk EUV Telescopes* (FET) of the TESIS solar observatory, namely, the FET-304/171 telescope (Kuzin *et al.*, 2009). This instrument was designed at the Lebedev Institute of the Russian Academy of Sciences and launched on board the *Complex ORbital Observations Near-Earth of Activity of the Sun-Photon* (CORONAS-*Photon*) satellite on 30 January 2009. To our advantage, CORONAS-*Photon*'s relatively short operation time (until mid January 2010) coincided with the end of an extraordinarily long solar minimum between Solar Cycles 23 and 24. This gave us an opportunity to unrestrictively observe small prominences, which are barely seen during the rest of the cycle against larger manifestations of solar activity. Here, we analyze the most complete portion of this dataset from August to November 2009, which is publicly available on-line at http://tesis.lebedev.ru.

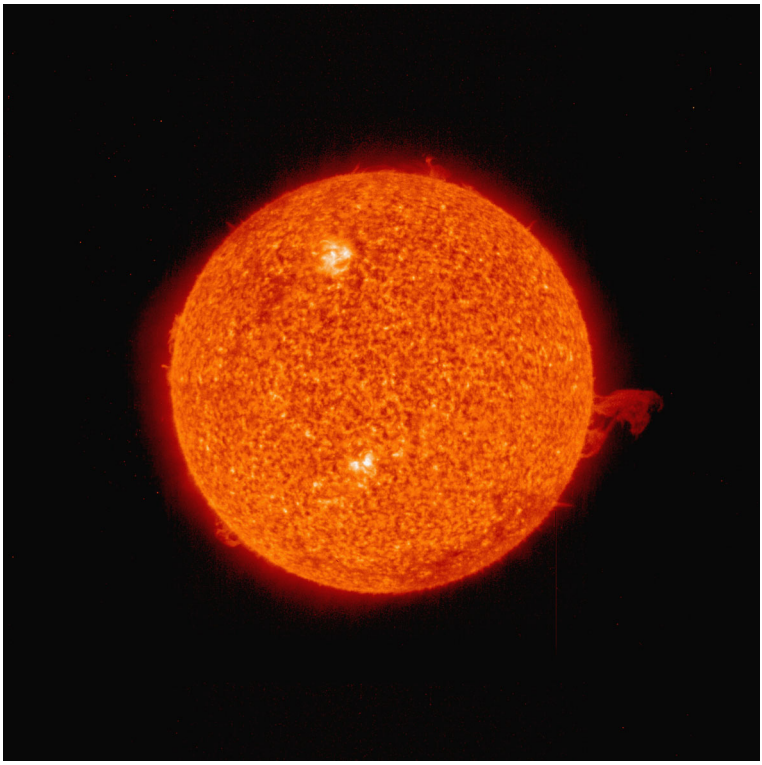

Figure 1 Example of typical TESIS observation in He II 304 Å line taken on 26 September 2009 at 15:44:46 UT (intensities are in logarithmic scale). Note that solar North is not up in the original images.

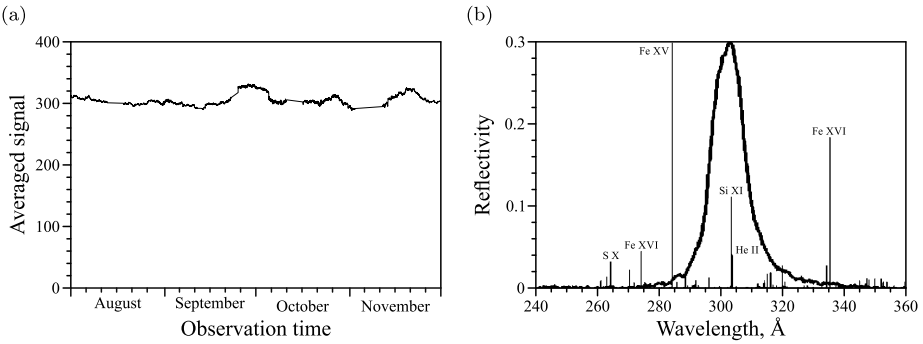

Figure 2 (a) Averaged signal from the CCD throughout the observation period; we have made the correction for varying Sun–Earth distance. (b) Spectral reflectivity of the focusing mirror in the 304 Å channel of TESIS and the corresponding EUV lines.

With a field of view of 1°, the telescope was able to image the full solar disk and the corona up to the distance of ~ 0.95 solar radii above the limb (see an example of a typical observation in Figure 1). It produced 2048×2048 images with a pixel size of ~ 1.7 arcsec, or roughly 1.25 Mm. Half of the images, however, have been reduced to 1024×1024 due to telemetry limitations. For the regular observations in the 304 Å channel the cadence was set to 4.0 min, but as the observations were non-continuous because of the partly Earth-shaded orbit of the satellite, the resulting mean cadence amounted to ~ 7.2 min. To make sure that the CCD showed no apparent signs of degradation during the observation period, which could affect our investigations, we calculated the average response of the CCD, shown in Figure 2a. It clearly indicates that possible degradation of the CCD is negligible against the larger variations in solar irradiation.

Since the entrance and detector filters of the telescope were relatively broad, dedicated mainly to block the strong white-light radiation from the Sun, the bandpass in the 304 Å channel of TESIS was predominantly defined by the spectral reflectivity of its focusing mirror, which is shown in Figure 2b (Kuzin *et al.*, 2011). This figure also indicates the main contributors to this relatively broad-band channel: the closely spaced Si XI line at 303.3 Å and He II line at 303.8 Å. Contribution of the Si XI line has been previously investigated by several authors, who have found it to be around 3 – 4 % for the on-disk quiet-Sun regions and more than 90 % for the coronal emission (Cushman and Rense, 1978; Thompson and Brekke, 2000). Since plasma conditions in prominences are similar to that of the quiet Sun, helium emission is typically dominant in them.

3. Image Processing

A total of 18812 valid images of the Sun in the He II 304 Å line were obtained during the specified period. As we mentioned above, processing such an amount of data, including detection of prominences and measurement of their parameters, is not feasible by hand. For this purpose, we have developed an automatic method that is capable of locating the prominences on individual 304 Å images, tracking these features throughout their lifespan, and determining their most important spatial and dynamic characteristics. The operational principle of this method is described below as a sequence of several processing steps.

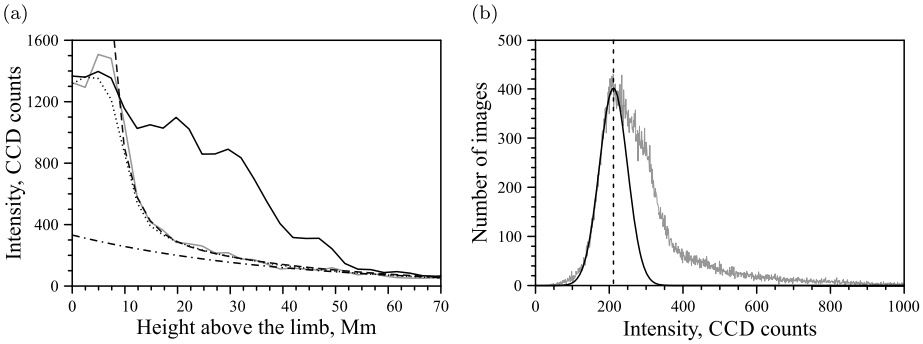

Figure 3 (a) Radial profiles of the quiet Sun (solid grey line), prominence (solid black line), statistically obtained background (dotted line), analytical fit to that background (dashed line), and its exponential part (dash-dotted line). (b) Intensity distribution at a fixed point of the corona (grey line) with an assumed Gaussian contribution from the quiet Sun (black line).

3.1. Preprocessing and Background Removal

In the preliminary stage, the data are prepared for subsequent operations: corrupted images are filtered out, and for the remainder corrections for minor defects are made (*e.g.*, hot pixels and cosmic ray hits). In addition, off-limb regions of the images are transformed to polar coordinates and stored as rectangular arrays to simplify further image processing (for an example, see Figure 4a).

Essentially, the next step would be to detect prominences on these pre-processed images. Unfortunately, as one can see from the Figure 3a, prominences are observed against a strong background, which can be attributed either to the thermal noise of the CCD and extra signal due to the scattered radiation, or to the radiation of the undisturbed corona itself. As Labrosse, Dalla, and Marshall (2010) rightly noted, to know the background is critical to the whole process. Analysis of individual images shows that this background does not change much with time, but is spatially highly inhomogeneous: it rapidly decreases with height and varies with latitude, having significant dips around the poles. To our advantage again, because the observation period is close to the solar minimum, the positions of the polar coronal holes remain stable in spite of the solar rotation. This allows us to determine the background following the statistical approach described below.

First, we use the whole dataset to build the intensity distribution of every individual pixel in the previously polar-transformed and aligned images, an example of which is shown in Figure 3b. We assume that in the quiet Sun, the observed intensity coming from a fixed point in the corona follows a normal distribution. This quiet-Sun distribution is supplemented with stronger signals coming from a small number of active features, which occasionally emerge in the corona. Therefore, we approximate the left slope of the obtained distribution with a Gaussian function and take the position of its maximum as the estimated value of background in that pixel.

To smooth out the noise and small-scale irregularities, we then look for an analytical function to fit the background we have thus obtained. After studying its radial and latitudinal profiles on semi-log and log–log plots, we have finally arrived at the following model:

$$B(\varphi, h) = a(\varphi)\mathrm{e}^{-b(\varphi)h + c(\varphi)\mathrm{e}^{-d(\varphi)h}}, \tag{1}$$

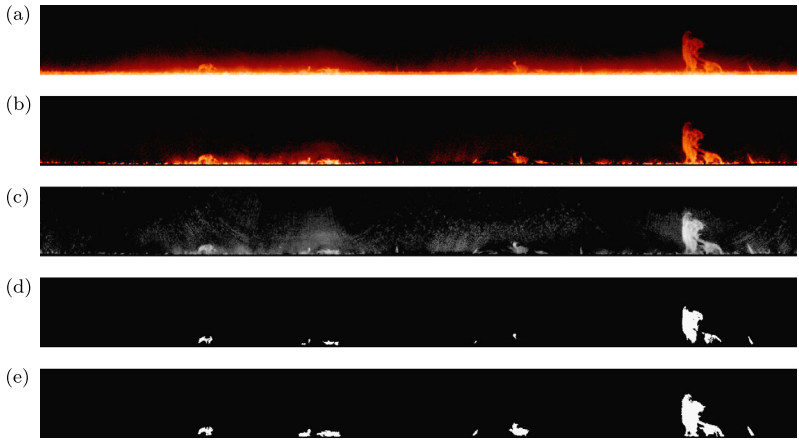

Figure 4 Processing steps of the image in Figure 1: (a) polar-transformed image with minor defects corrected, latitudes counted clockwise from the North pole, (b) background subtracted, (c) normalized image, (d) kernels used for the subsequent region-growing procedures, (e) final selections. Intensities in panels a to c are in logarithmic scale.

where h is the height above the limb, φ is the heliographic latitude, and $a(\varphi)$, $b(\varphi)$, $c(\varphi)$ and $d(\varphi)$ are generalized logistic functions of a similar form, *e.g.*

$$a(\varphi) = a_1 + \frac{a_2 - a_1}{\mathrm{e}^{(\varphi_0 - |\varphi|)/\delta\varphi} + 1}. \tag{2}$$

In other words, $a(\varphi)$ is equal to a_1 at the equator and middle latitudes and to a_2 in the vicinity of the poles, with a smooth transition from a_1 to a_2 centred at the latitude φ_0, the steepness of this transition determined by $\delta\varphi$. Parameters φ_0 and $\delta\varphi$ are taken the same for all four functions. Although the double exponent in Equation (1) may seem strange at first glance, it proved to be the best approximation to the specific radial profiles of the background obtained for this dataset; while $B(h)$ has an almost exponential dependence at higher altitudes, it becomes much steeper close to the limb (Figure 3a). Below a height of ~ 15 Mm the background is mostly due to the strong radiation from the EUV spicules, and prominences are in general not visible there. Therefore, we do not attempt to fit this part with an analytical function.

Subsequently, we follow a technique similar to that described in Morgan, Habbal, and Woo (2006), and use this modelled background B to normalize every image in the dataset according to the equation

$$N = \frac{I + \delta}{B + \delta} = 1 + \frac{I - B}{B + \delta}, \tag{3}$$

where $I = I(\varphi, h)$ is a given polar-transformed image and $N = N(\varphi, h)$ is the same image after normalization (see an example in Figure 4c). We introduce here a small parameter δ, first, to avoid division by zero, and second, to suppress the noise at higher altitudes, where B is close to zero. Thus, it must be substantially greater than the average noise level in the periphery of the image (~ 5 CCD counts for this instrument) and substantially smaller than typical signal values from prominences (~ 100 and more CCD counts). For the dataset employed, we have set δ equal to 25.

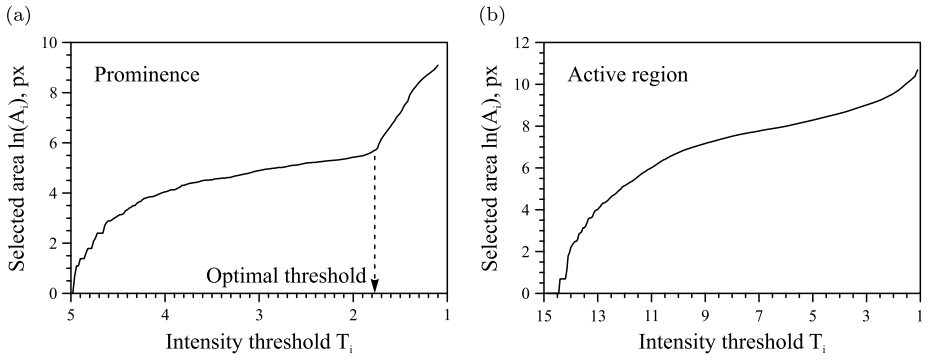

Figure 5 Selected area A_i as it grows with the decrease of the cut-off threshold T_i for a prominence (a) and an active region (b).

3.2. Prominence Detection in the Individual Images

To avoid restrictions imposed by the necessity of simultaneous multi-wavelength observations, our first concern was to be able to detect prominences using 304 Å observations only. The problem is, however, that they are not the only bright structures seen off-limb in this usually broad-band channel. High coronal temperatures above the active regions (ARs) can stimulate emission in the Si XI line and cause a considerable increase in brightness above the limb. Consequently, additional procedures are required to distinguish between true prominences and these AR-imposed effects. A number of solutions to this problem have previously been proposed by several authors. Foullon and Verwichte (2006), for example, implemented a histogram segmentation to set an intensity threshold for an individual image and then employed multi-wavelength observations to discard active regions. Wang *et al.* (2010) first selected potential prominences by a preset threshold and then performed a regression analysis based on the shape of the selected regions. A disadvantage of this method is, however, that incorrect thresholding may lead to misclassification and therefore to no prominence detection. Finally, an interesting method was proposed by Labrosse, Dalla, and Marshall (2010); these authors used moments to find radial profiles characteristic only of prominences and then reconstructed their shape by morphological opening procedures.

We have developed a different technique, taking advantage of the fact that in the He II 304 Å line quiescent prominences tend to have sharp boundaries (at least in the dataset concerned), and in contrast, active regions reveal themselves off-limb as diffuse brightenings. In our study, we mainly concentrate on the measurement of the physical parameters of prominences for the later statistical treatment. Thus, our primary concern was to achieve high precision in prominence detection to derive their properties most reliably. To meet this requirement, our algorithm individually determines an optimal threshold for each prominence on the image by the following procedure.

First, to isolate individual features off-limb, kernels of future prominences are selected as the areas where the normalized signal N is greater than a fixed threshold $T_{\mathrm{kern}} = 3.0$. Each kernel is then treated separately and expanded by means of the region-growing procedure. This operation is performed multiple times with a varying cut-off threshold T_i, which is gradually decreased from $T_{\max} = 7.0$ to $T_{\min} = 1.1$ at an increment of $\delta T = -0.02$. Concurrently, the area of the resulting selection A_i is measured as a function of T_i. Naturally, as T_i decreases, A_i grows monotonically; a typical view of this dependence is shown in Figure 5a. One can notice that T_i can be greater than T_{kern}; in this case, the region-growing procedure is

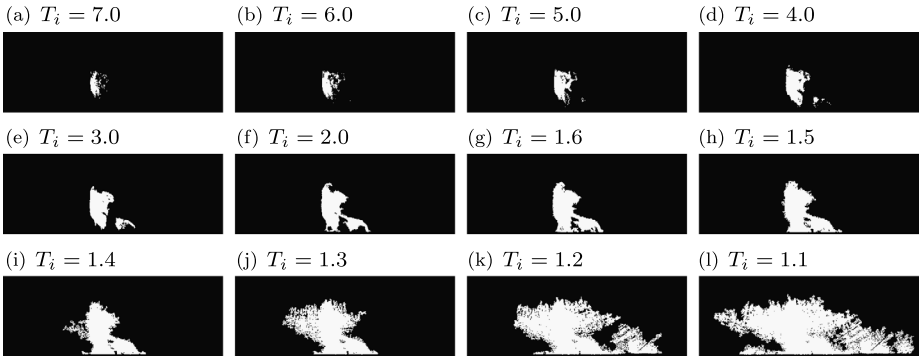

Figure 6 Resulting selection at several stages of the iterative region-growing procedure.

reduced to finding all the fitting points inside the kernel. In addition, if in the region-growing process two kernels merge together, their measured dependencies $A_i(T_i)$ are summed.

Initially, when the main body of a prominence is being selected, A_i grows quite rapidly (Figures 6a – d). Later, when the sharp boundaries of the prominence are reached, the increase of A_i slows down (Figures 6e – h); this is easily identifiable in Figure 5a as some sort of a saturation plateau. Finally, when T_i becomes sufficiently low such that regions surrounding the prominence begin to be selected, A_i bursts to a rapid growth (Figures 6i – l). The value of T_i preceding this burst is then chosen as an optimal intensity threshold for the given prominence.

The main advantage of this approach is the high dynamic range of detection, which is well illustrated by Figure 7. At the late stages of eruption the faint prominence material is detected just as well as the bright body of the prominence before the eruption has started. Another important feature of this technique is that it allows the direct distinction between prominences and active regions. As the latter have no sharp boundaries, the dependence $A_i(T_i)$ is smoother, with no characteristic knee as is the case of a prominence (Figure 5b). Therefore, no optimal threshold is determined, and they are not detected as prominences. This, of course, inhibits the detection of active prominences, which are often inseparable from the active regions, but as we stated above, they are not the subject of the present study.

We should note that this technique is still biased by the arbitrary choice of T_{kern}. Fortunately, this parameter should be chosen such that it would fall into the saturation plateau in Figure 5a, which precedes the burst of the selected area. Since the plateau is broad enough, there is no difficulty in choosing T_{kern}, which will fall into this interval for most of the prominences. Therefore, small variations of T_{kern} are probably not relevant for the algorithm performance. When testing the algorithm, we eventually chose $T_{\mathrm{kern}} = 3.0$ since it produced better results for a small portion of the dataset that we have studied manually. As for the computational efficiency of the algorithm, the most time-consuming operation is the iterative region-growing procedure described above. However, since each successive iteration does not expand the initial seed, but continues to expand the result of the previous iteration, the whole process can be interpreted as a single process, with a number of intermediate stops at certain thresholds. Therefore, the actual processing time is much shorter than that required to preform the same number of independent region-growing procedures. In our case, the processing of each image took typically from two to three seconds on a 3.1 GHz eight-core CPU, depending on the number of kernels initially selected by the algorithm.

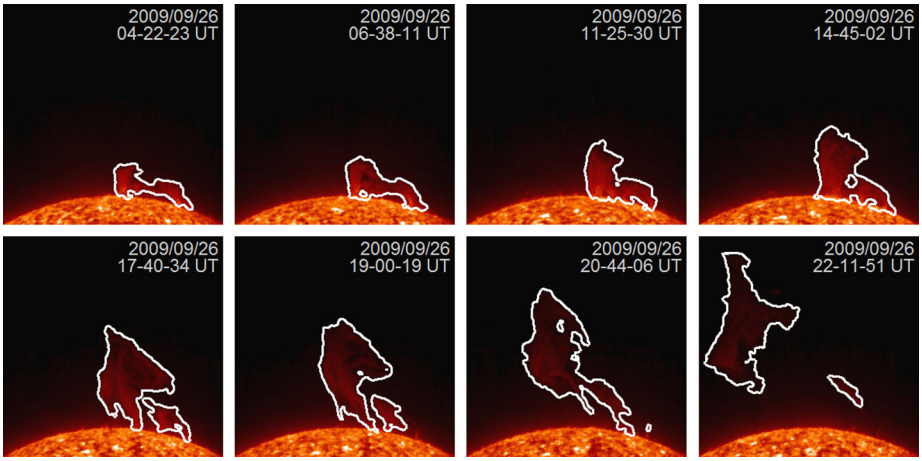

Figure 7 The high dynamic range of detection exemplified by a large eruptive event observed on the north-eastern limb on 26 September 2009. The result of the detection is outlined with a bright curve; the intensities are in logarithmic scale.

3.3. Parameter Extraction, Event Tracking, and Catalogue Compilation

When all prominences are duly located on the image, for each of them the algorithm determines the heliographic latitude and altitude of the highest point and calculates its visible (*i.e.* projected) area, integral brightness, and position of the centroid. Furthermore, a set of models described below in Section 4.2 is used to estimate its volume, mass and, therefore, its gravitational (potential) energy. Additionally, to find the erupted parts of prominences, selections that are detached from the disk and are entirely located above a certain height of 30 Mm are marked.

Finally, the last step of our algorithm is to track prominences as they appear on a series of consecutive images. We note that most of the prominences are confined to the same latitudes during their entire lifetime. Therefore, two prominences can be considered a single event if they overlap on two or more consecutive images. They can be absent, however, on no more than two images in a row and must be observed on at least three images. After tracking a prominence with this approach, the algorithm registers the moment of its appearance and disappearance and calculates its lifetime and the number of images in which it was detected. For all of the characteristics of a prominence determined previously in the individual images, the minimum, the maximum, the average, and the standard deviation are found. After that, tangential and radial velocities of the centroid of a prominence are calculated based on the change of its position, as well as the radial velocity of the highest point of the prominence. Finally, if the tracked prominence at any time had regions that were marked as erupted, the whole event is classified as an eruptive prominence. All of these data are stored in a table or a catalogue, which is the final result of the application of the algorithm. In the next section, we continue our investigation with the analysis of a catalogue, which was thereby obtained for the observation period.

To evaluate the accuracy of the detection, we manually investigated a relatively short period of ten days from 10 to 20 September 2009. During this period, a total of 46 prominences was detected. We found observable prominences in the images for 42 of these detections, although some of them were barely distinguishable by eye. For the remaining four, we could

find no features resembling an off-limb prominence. Most likely, these false detections resulted from the increased coronal radiation due to the presence of an inter-network bright point close to the limb, or from a superposition of short-lived and small-scale phenomena, such as surges and polar macrospicules. At the same time, we found no large prominences that were not detected by the algorithm; it is still possible, however, that we could have missed several rather small ones. In addition, all 42 prominences were correctly classified by the algorithm as either stable or eruptive (although for smaller prominences it proved to be harder to draw this distinction). The algorithm was sometimes unable to detect faint remainders or precursors of the prominences, therefore the derived lifetimes are most likely to be underestimated.

4. Results

4.1. Dynamics and Morphology

For a period of four months, we detected a total of 389 quiescent prominences, 41 of them were classified as eruptive. The detected prominences vary largely in size, the largest being 500 Mm long and 150 Mm high and the smallest 25 Mm both in length and height (Figures 8a, b). Thus, the characteristic size of a prominence $\widetilde{L} = \sqrt{LH}$ (where H is the prominence height and L is the prominence length along the limb) is smaller than 70 Mm for 50 % of the prominences. We find that most of the detected prominences are stretched along the limb; for only 10 % the ratio L/H was found to be lower than 1 (Figure 8c). As for latitudinal distribution, more than 95 % of the prominences are concentrated at latitudes below $\pm 60^\circ$, with the highest probability density falling at medium latitudes around $\pm 40^\circ$ (Figure 8d).

Most of the detected prominences proved to be stable, showing practically no apparent bulk motion. This is well demonstrated by Figure 8e; for more than 92 % of the prominences the centroid velocity, averaged over the prominence lifetime, does not exceed 3 $\mathrm{km\,s^{-1}}$. This value, however, does not reveal the inner plasma motions in prominences. A surprising result is that around 75 % of the prominences were detected off-limb for less than 24 hours (Figure 8f). Manual investigation has shown that smaller prominences tend to be more dynamic than the larger ones and often disappear from the limb much faster than what the solar rotation would imply. Finally, it was found that eruptive prominences in general show the same distribution of the inferred parameters, except for the fact that they tend to be among the larger prominences. This suggests the existence of a certain critical mass that needs to be reached before a prominence can become unstable.

4.2. Estimation Models

In contrast to determining spatial and dynamic characteristics, estimating the mass and, consequently, the gravitational energy of prominences proves to be a much more difficult task. The most precise methods developed so far are generally based on measuring the fraction of background radiation absorbed by a prominence, most commonly in the iron EUV lines (Gilbert, Holzer, and MacQueen, 2005; Schwartz *et al.*, 2012). Unfortunately, this approach can only be used in a limited number of cases, when prominences are observed against a sufficiently uniform background that does not change much over time. We attempted, however, to apply this technique using the 171 Å channel data of TESIS, but as expected, with no promising result. Interesting developments to this method have been proposed by Landi

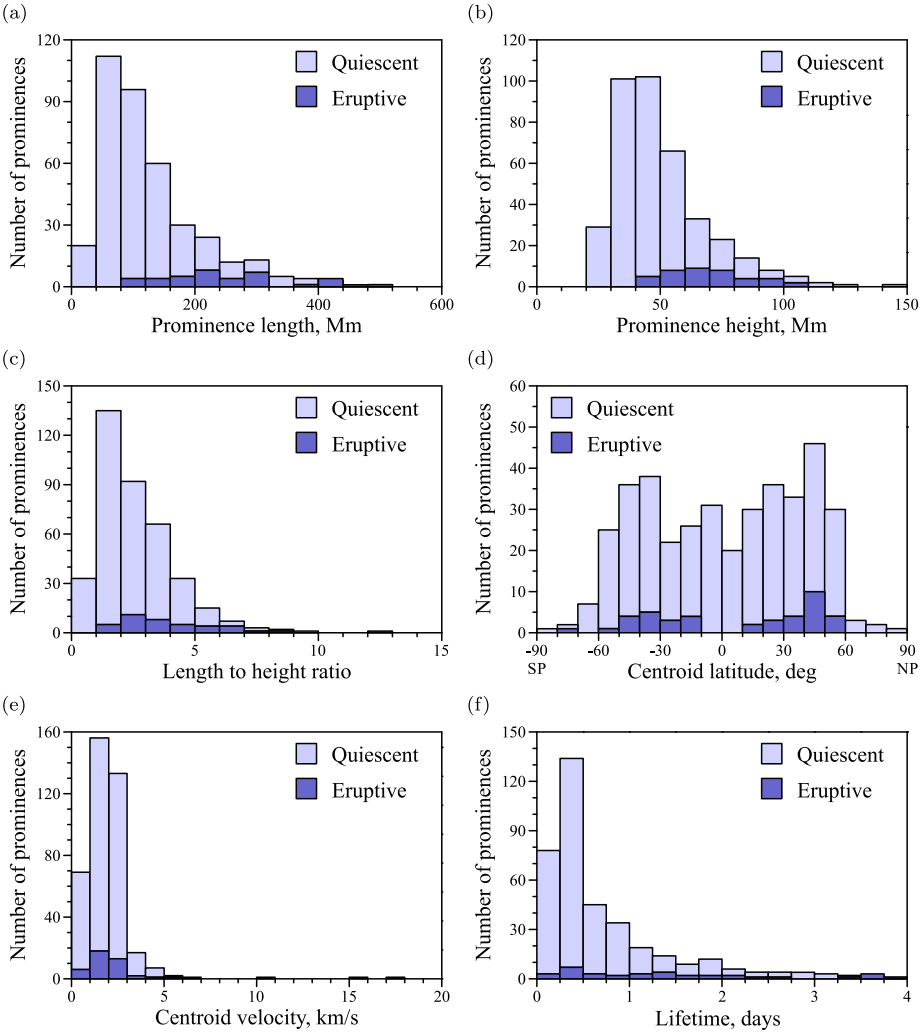

Figure 8 (a) Distribution of the lengths of prominences. (b) Distribution of the heights above solar limb. (c) Distribution of the shapes in terms of length to height ratio. (d) Latitudinal distribution of prominences; negative latitudes correspond to the southern hemisphere, positive to the northern hemisphere. (e) Distribution of centroid velocities. (f) Distribution of observed lifetimes. The parameters in panels a – e are averaged over the prominence lifetime.

and Reale (2013) and Williams, Baker, and van Driel-Gesztelyi (2013). These authors employed observations in several EUV lines with different absorption coefficients to exclude redundant parameters and thus to achieve higher precisions. Both these techniques, however, require prominence material to be cool enough so that it would not emit in the He II 304 Å line. Low, Fong, and Fan (2003) have also proposed to estimate a prominence mass as the minimum amount of plasma needed to maintain a stable current magnetic configuration; evidently, this approach is not applicable to our case either. Thus, we have no better option than to limit our study with only rough estimates of prominence masses and energies. Although inapplicable for the detailed studies of prominences, such estimates can be fairly

useful for investigating the general properties of a substantial number of events, which can not be studied individually.

In our attempt to estimate the mass of a prominence, we rely on the fact that the prominence plasma proves to be optically thick when observed in the He II 304 Å line. This implies that the observed radiation is mainly formed in an outer layer of thickness L_0, where the radiation from the underlying layers of the prominence is absorbed by helium ions. From the Beer-Lambert law, the thickness L_0 is related to the mean number density of partly ionized helium atoms n_{HeII} as

$$L_0 \sim 1/\varepsilon \sim 1/n_{\mathrm{HeII}}, \tag{4}$$

where ε is the mean absorption coefficient of the emitting layer along the line of sight. We therefore assume that this outer layer is isothermal (with temperature T_0) and homogeneous along the line of sight, which means that the observed flux F is given by

$$F = G(T_0)\mathrm{EM}(T_0) \sim n_{\mathrm{HeII}} n_{\mathrm{e}} L_0 \sim n_{\mathrm{e}}, \tag{5}$$

where n_{e} is the electron density, G is the contribution function, and EM is the emission measure. Numerical simulations by Gouttebroze and Labrosse (2009), which consider a much more realistic radiation transfer, including scattering of incident radiation from the Sun, imply a more complex dependence. However, for typical plasma temperatures and densities in prominences these simulations suggest that a linear dependence as in Equation (5) is an acceptable approximation.

In the simplest case, the volume of a prominence, V, can be related to its observed area, A, as $V \sim A^{3/2}$. Here, we use an alternative method instead and estimate the thickness of a prominence, D, at each pixel of the detected area assuming that prominences have a more or less round section. This means that the prominence attains its maximum thickness $D_{\max}$ at points that are the most distant from the boundaries and that $D_{\max}$ is equal to twice that distance. For the rest of the pixels, we calculate the thickness D as

$$D = 2\sqrt{D_{\max}^2 - (D_{\max} - R)^2}, \tag{6}$$

where R is the minimal distance from the given point to the prominence edge. However, during our study, we have found that for the set of detected prominences this method gives a clear dependence $V \sim A^{1.33\pm0.07}$, which is more consistent with the fact that prominences tend to be elongated rather than spherical in shape. Both methods, however, are far from being precise as they do not take into account projection effects and, again, can only be used for a rough evaluation.

These two models allow us to obtain estimates of the mass and, therefore, of the gravitational energy of a detected prominence. We choose the proportionality coefficient in Equation (5) such that, for all the detected prominences, the mean value of the electron density would equal a typical value of 2×10^{10} cm^{-3}, which was found in previous studies of individual prominences (Bommier, Leroy, and Sahal-Brechot, 1986; Bommier *et al.*, 1994; Wiik, Heinzel, and Schmieder, 1994). We have to assume here, of course, that the electron density inside a prominence remains proportional to that in its outer shell along the line of sight. Earlier studies of prominences have shown that their ionisation degree is typically in the range of 0.5 – 0.8 (Orrall and Schmahl, 1980; Kanno, Withbroe, and Noyes, 1981) and the helium abundance is around 0.1 (Heasley and Milkey, 1978). Therefore, suggesting that most of the prominence mass is due to the hydrogen atoms, and the low helium abundance will not imply a large error, we calculate the mean density of the prominence plasma by

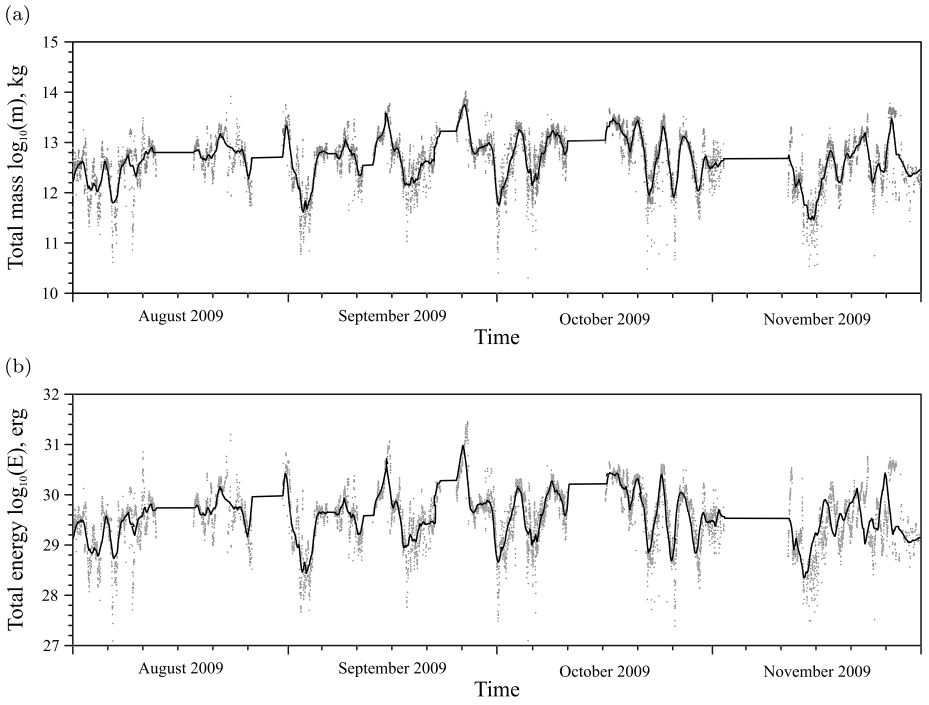

Figure 9 Total mass (a) and gravitational energy (b) of prominences simultaneously observed in a single image as they vary through the observation period. Grey dots correspond to individual images, and the black line is the one-day smoothed trend.

multiplying the inferred electron density by the proton mass. Subsequently, multiplying this plasma density by the previously calculated thickness of the prominence, we obtain the column mass at the every point of its visible surface. Thus, we can obtain the total mass of a prominence by integrating these column masses over the observed area of a prominence, and the gravitational energy by integrating the column masses multiplied by the gravitational potential (here, we assume that the detected prominences are in the plane of the sky). This is, by no means, a precise method, but with the data available, it remains suitable for rough estimates of these important values.

4.3. Mass and Gravitational Energy

After summing masses and energies of all individual prominences detected in a single image, we can calculate the total mass of prominences observed simultaneously off-limb. During the observation period, the total mass of the prominences varied greatly with time between $10^{12.2}$ and $10^{13.6}$ kg (Figure 9a), as well as the total gravitational energy, which was found to be in the range from $10^{28.7}$ up to $10^{30.4}$ erg (Figure 9b).

In effect, we can observe, and therefore detect, only a certain fraction of all prominences simultaneously present on the Sun, which are located close to the limb and are high enough to be seen off-limb at their position. To estimate this fraction, we develop a simple geometrical model presented in Figure 10. Here, a prominence BT, which has a typical height h_0, is located at a critical position where it becomes no more visible above the limb. We can

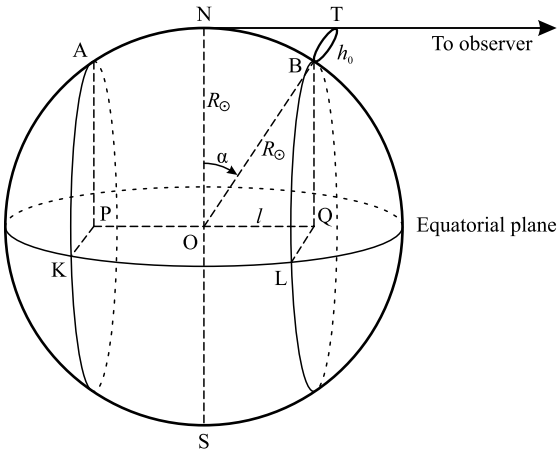

Figure 10 Geometrical model used to evaluate the fraction of prominences visible off-limb. The prominence BT is located at a critical position, where it may become not visible above the limb.

assume $h_0 \simeq 40$ Mm, taking the most probable value from the distribution in Figure 8b; however, since prominences are not visible below ~ 15 Mm because of strong background radiation from the EUV spicules, we take here $h_0 = 25$ Mm and the solar radius $R_\odot = 715$ Mm. According to this model, we are able to observe only those prominences that are located between the planes APK and BQL (Figure 10). The area of the solar surface confined between these two planes is given by

$$A_{\rm vis} = 2\pi R_\odot 2l = 4\pi R_\odot^2 \sin\alpha, \tag{7}$$

where $2l = \mathrm{PQ}$ and α is the $\widehat{\mathrm{NOB}}$. Since $4\pi R_\odot^2$ is the total surface area of the Sun, we can observe off-limb a fraction of around

$$\sin\alpha = \sqrt{1 - R_\odot^2/(R_\odot + h_0)^2} \simeq \sqrt{2h_0/R_\odot} \simeq 0.25 \tag{8}$$

of all prominences present anywhere on the Sun, including those visible as filaments on the disk. Taking this into account, we conclude that at solar minimum, all quiet-Sun prominences simultaneously contain about $10^{12}-10^{14}$ kg of plasma, and their total gravitational energy is of the order of $10^{29}-10^{31}$ erg.

In addition, the large number of detected events enables us to investigate the form of their gravitational energy spectrum, which is shown in Figure 11a. Although this spectrum may be shifted towards lower or higher energies due to the arbitrary choice of the coefficient in Equation (5), its shape is only biased by our assumptions about the prominence morphology and density distribution along the line of sight. The main feature of this spectrum is the clear maximum at around $10^{28.6}$ erg. This behaviour might be explained by the existence of a low sensitivity threshold in our algorithm. Most likely, we are not able to detect small and low-lying prominences in the 304 Å images, as they become barely distinguishable from the strong background below 15 Mm (Figure 3a). Indeed, we detected no prominences lower than 20 Mm (Figure 8b). On the other hand, there might be no such small prominences at all, as they may become unstable at these spatial scales or indistinguishable from smaller objects seen above the limb. If so, the conventional definition of a prominence becomes no more applicable in this case. At this point, we only consider the part of the spectrum above $10^{28.6}$ erg to have a physical meaning. In a log–log plot (Figure 11b), it shows a clear power-law dependence, its index given by the slope of the distribution that we find to be -1.1 ± 0.2.

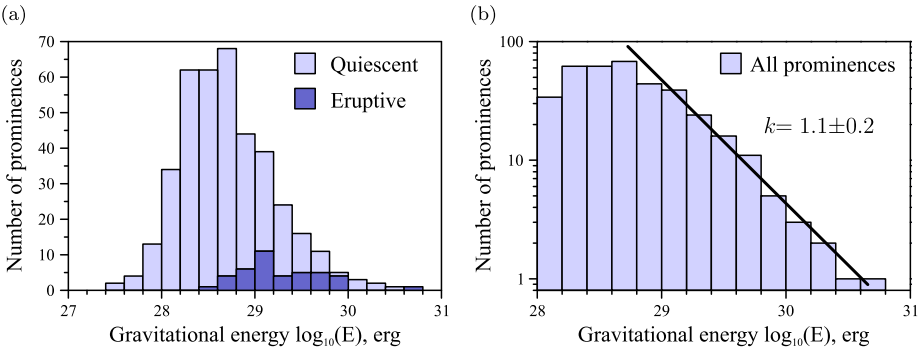

Figure 11 (a) Gravitational energy spectrum of the prominences. (b) The slope of the same distribution for a limited energy range in a log–log scale.

Hence, in this case, the power-law index is close to -1, which means that at least within the sensitivity range of our method, the gravitational energy is close to be evenly distributed among prominences of different sizes.

5. Discussion

As we mentioned above, most of the previous studies of prominences were limited to particular cases, in general to the largest events, which are easier to identify by eye. At the same time, the whole set of prominences is of great interest, and several questions remain, to which answers cannot be given by studies of individual events. It is unclear, for example, how the physical properties of prominences vary from one to the other and what their long-term behaviour is, *i.e.*, how they change throughout the solar cycle (for a discussion, see a review by Patsourakos and Vial, 2002). Detailed catalogues that give not only qualitative, but also quantitative information and comprise a significant number of their measurable parameters would enable us to perform large statistical studies of these phenomena. These studies, perhaps being not as precise as the individual ones, allow us, however, to cover a much wider range of events, maintaining a consistent point of view, less dependent on the selection of the objects examined.

A catalogue of prominences above the limb would also be an appropriate complement to the existing catalogues of filaments on disk (Zharkova *et al.*, 2005), as they show prominences in two orthogonal projections. Equally promising are combined analyses of prominence catalogues with those of associated events in the solar corona. For example, deeper conclusions can be achieved by combining prominence catalogues and existing CME catalogues (Gopalswamy *et al.*, 2009; Robbrecht, Berghmans, and Van der Linden, 2009; Floyd *et al.*, 2013). They are both observed in the direction orthogonal to the line of sight, and comparative studies of a great number of events would help advance our understanding of the mechanisms underlying CME initiation. A joint study including flare catalogues (Watanabe, Masuda, and Segawa, 2012; Aschwanden *et al.*, 2014) would be of no less interest, as prominence eruptions are often an essential part of these complex processes.

Within the limits of this study, we have investigated a relatively short period. Nevertheless, it provides much new information about general properties of the entire set of prominences, including rather small ones. One should also note that this observation period coincides with the end of an extraordinarily long solar minimum, which is a unique event by

itself. The main advantage of the algorithm developed is a well-founded technique of background removal and a more accurate reconstruction of prominences, which increases the reliability of the measured prominence properties. Moreover, this algorithm is able to distinguish between the prominence and off-limb manifestations of active regions without the need of learning the method previously or using multi-wavelength observations.

The obtained values of mass and gravitational energy of prominences, despite the simplicity of the evaluation method used, are nevertheless the first attempt to determine these important properties for a substantial number of prominences. These data are useful to constrain existing models of prominence formation and evolution and to study their role in the general mechanisms of mass and energy transfer in the solar corona. It is also relevant that these properties are not only obtained for the largest events, but for the whole ensemble. Therefore, they give an early insight into how these parameters are distributed among prominences of different sizes.

Because of the relatively short operation time of TESIS, our next goal is to adapt our algorithm to process the data obtained by other instruments, primarily those on board SDO. These data will permit us to examine prominences on a much longer time scale and thus to detect long-term variations of their properties throughout the solar cycle, if any, and to find out why this solar minimum was so different from the others. For now, we can see two major obstacles that we will face in this endeavour. First, our study did not include active prominences, as they were not numerous during the examined period. Closer to the solar maximum, however, the number of this type of prominences will greatly increase along with the general increase of solar activity. Nevertheless, we believe that our algorithm can be successfully used to detect these prominences as well, against the enhanced active region background. The other problem is that our method of determining the background becomes inapplicable because of the more complex morphology of the corona during the rest of the solar cycle. Hopefully, the statistical approach used here remains a powerful tool to deal with this problem as well.

Acknowledgements This work was supported by the Russian Foundation for Basic Research (grant 14-02-00945) and by the Program No. 9 for fundamental research of the Presidium of the Russian Academy of Sciences. We are grateful to all members of the TESIS development team who have put much effort in the design and operation of this instrument.

References

Aschwanden, M.J., Wülser, J.P., Nitta, N.V., Lemen, J.R., Freeland, S., Thompson, W.T.: 2014, STEREO/Extreme Ultraviolet Imager (EUVI) event catalog 2006 – 2012. *Solar Phys.* **289**, 919. DOI.

Bommier, V., Leroy, J.L., Sahal-Brechot, S.: 1986, The linear polarization of hydrogen H-beta radiation and the joint diagnostic of magnetic field vector and electron density in quiescent prominences – Part two – The electron density. *Astron. Astrophys.* **156**, 90.

Bommier, V., Landi Degl'Innocenti, E., Leroy, J.L., Sahal-Brechot, S.: 1994, Complete determination of the magnetic field vector and of the electron density in 14 prominences from linear polarization measurements in the HeI D3 and H-alpha lines. *Solar Phys.* **154**, 231. DOI.

Cushman, G.W., Rense, W.A.: 1978, Solar He II 304 Å and SI XI 303 Å line profiles. *Solar Phys.* **58**, 299. DOI.

Filippov, B., Koutchmy, S.: 2008, Causal relationships between eruptive prominences and coronal mass ejections. *Ann. Geophys.* **26**, 3025. DOI.

Floyd, O., Lamy, P., Boursier, Y., Llebaria, A.: 2013, ARTEMIS II: A second-generation catalog of LASCO coronal mass ejections including mass and kinetic energy. *Solar Phys.* **288**, 269. DOI.

Foullon, C., Verwichte, E.: 2006, Automated detection of EUV prominences. *Solar Phys.* **234**, 135. DOI.

Galsgaard, K., Longbottom, A.W.: 1999, Formation of solar prominences by flux convergence. *Astrophys. J.* **510**, 444. DOI.

Gilbert, H.R., Holzer, T.E., MacQueen, R.M.: 2005, A new technique for deriving prominence mass from SOHO/EIT Fe XII (19.5 nanometers) absorption features. *Astrophys. J.* **618**, 524. DOI.
Gilbert, H.R., Holzer, T.E., Burkepile, J.T., Hundhausen, A.J.: 2000, Active and eruptive prominences and their relationship to coronal mass ejections. *Astrophys. J.* **537**, 503. DOI.
Gopalswamy, N., Shimojo, M., Lu, W., Yashiro, S., Shibasaki, K., Howard, R.A.: 2003, Prominence eruptions and coronal mass ejection: A statistical study using microwave observations. *Astrophys. J.* **586**, 562. DOI.
Gopalswamy, N., Yashiro, S., Michalek, G., Stenborg, G., Vourlidas, A., Freeland, S., Howard, R.: 2009, The SOHO/LASCO CME catalog. *Earth Moon Planets* **104**, 295. DOI.
Gouttebroze, P., Labrosse, N.: 2009, Radiative transfer in cylindrical threads with incident radiation. VI. A hydrogen plus helium system. *Astron. Astrophys.* **503**, 663. DOI.
Heasley, J.N., Milkey, R.W.: 1978, Structure and spectrum of quiescent prominences. III – Application of theoretical models in helium abundance determinations. *Astrophys. J.* **221**, 677. DOI.
Heinzel, P.: 2007, Multiwavelength observations of solar prominences. In: Demircan, O., Selam, S.O., Albayrak, B. (eds.) *Solar and Stellar Physics Through Eclipses*, *Astron. Soc. Pacific C.S.* **370**, 46.
Hirayama, T.: 1985, Modern observations of solar prominences. *Solar Phys.* **100**, 415. DOI.
Kanno, M., Withbroe, G.L., Noyes, R.W.: 1981, Analysis of extreme-ultraviolet spectroheliograms of solar prominences. *Solar Phys.* **69**, 313. DOI.
Kuzin, S.V., Bogachev, S.A., Zhitnik, I.A., Pertsov, A.A., Ignatiev, A.P., Mitrofanov, A.M., Slemzin, V.A., Shestov, S.V., Sukhodrev, N.K., Bugaenko, O.I.: 2009, TESIS experiment on EUV imaging spectroscopy of the Sun. *Adv. Space Res.* **43**, 1001. DOI.
Kuzin, S.V., Zhitnik, I.A., Shestov, S.V., Bogachev, S.A., Bugaenko, O.I., Ignat'ev, A.P., Pertsov, A.A., Ulyanov, A.S., Reva, A.A., Slemzin, V.A., Sukhodrev, N.K., Ivanov, Y.S., Goncharov, L.A., Mitrofanov, A.V., Popov, S.G., Shergina, T.A., Solov'ev, V.A., Oparin, S.N., Zykov, A.M.: 2011, The TESIS experiment on the CORONAS-PHOTON spacecraft. *Solar Syst. Res.* **45**, 162. DOI.
Labrosse, N., Dalla, S., Marshall, S.: 2010, Automatic detection of limb prominences in 304 Å EUV images. *Solar Phys.* **262**, 449. DOI.
Labrosse, N., Gouttebroze, P.: 2001, Formation of helium spectrum in solar quiescent prominences. *Astron. Astrophys.* **380**, 323. DOI.
Labrosse, N., Heinzel, P., Vial, J.C., Kucera, T., Parenti, S., Gunár, S., Schmieder, B., Kilper, G.: 2010, Physics of solar prominences: I – Spectral diagnostics and non-LTE modelling. *Space Sci. Rev.* **151**, 243. DOI.
Landi, E., Reale, F.: 2013, Prominence plasma diagnostics through extreme-ultraviolet absorption. *Astrophys. J.* **772**, 71. DOI.
Leroy, J.L., Bommier, V., Sahal-Brechot, S.: 1984, New data on the magnetic structure of quiescent prominences. *Astron. Astrophys.* **131**, 33.
Lin, J., Soon, W., Baliunas, S.L.: 2003, Theories of solar eruptions: A review. *New Astron. Rev.* **47**, 53. DOI.
Low, B.C., Fong, B., Fan, Y.: 2003, The mass of a solar quiescent prominence. *Astrophys. J.* **594**, 1060. DOI.
Mackay, D.H., Karpen, J.T., Ballester, J.L., Schmieder, B., Aulanier, G.: 2010, Physics of solar prominences: II – Magnetic structure and dynamics. *Space Sci. Rev.* **151**, 333. DOI.
Morgan, H., Habbal, S.R., Woo, R.: 2006, The depiction of coronal structure in white-light images. *Solar Phys.* **236**, 263. DOI.
Orrall, F.Q., Schmahl, E.J.: 1980, The H I Lyman continuum in solar prominences and its interpretation in the presence of inhomogeneities. *Astrophys. J.* **240**, 908. DOI.
Patsourakos, S., Vial, J.C.: 2002, Soho contribution to prominence science. *Solar Phys.* **208**, 253. DOI.
Pettit, E.: 1932, Characteristic features of solar prominences. *Astrophys. J.* **76**, 9. DOI.
Robbrecht, E., Berghmans, D., Van der Linden, R.A.M.: 2009, Automated LASCO CME catalog for solar cycle 23: Are CMEs scale invariant? *Astrophys. J.* **691**, 1222. DOI.
Schwartz, P., Fárník, F., Heinzel, P., Kotrč, P., Anzer, U.: 2012, Mass of solar prominences estimated from multi-wavelength data. In: Sekii, T., Watanabe, T., Sakurai, T. (eds.) *Hinode-3: The 3rd Hinode Science Meeting*, *Astron. Soc. Pacific C.S.* **454**, 117.
Severny, A.B., Khokhlova, V.L.: 1953, Study of motion and emission of solar prominences. *Izv. Krym. Astrofiz. Obs.* **10**, 9.
Tandberg-Hanssen, E.: 1995, *The Nature of Solar Prominences*, *Astrophys. Space Sci. Lib.* **199**, Kluwer Academic, Dordrecht.
Thompson, W.T., Brekke, P.: 2000, EUV full-Sun imaged spectral atlas using the SOHO coronal diagnostic spectrometer. *Solar Phys.* **195**, 45. DOI.
van Ballegooijen, A.A., Martens, P.C.H.: 1989, Formation and eruption of solar prominences. *Astrophys. J.* **343**, 971. DOI.

Wang, Y., Cao, H., Chen, J., Zhang, T., Yu, S., Zheng, H., Shen, C., Zhang, J., Wang, S.: 2010, Solar limb prominence catcher and tracker (SLIPCAT): An automated system and its preliminary statistical results. *Astrophys. J.* **717**, 973. DOI.

Watanabe, K., Masuda, S., Segawa, T.: 2012, Hinode flare catalogue. *Solar Phys.* **279**, 317. DOI.

Wiik, J.E., Heinzel, P., Schmieder, B.: 1994, Electron densities in solar prominences. In: Rusin, V., Heinzel, P., Vial, J.C. (eds.) *IAU Coll. 144: Solar Coronal Structures*, 381.

Williams, D.R., Baker, D., van Driel-Gesztelyi, L.: 2013, Mass estimates of rapidly moving prominence material from high-cadence EUV images. *Astrophys. J.* **764**, 165. DOI.

Zhang, Y.Z.: 2013, The formation and eruption of solar quiescent prominences. *Astrophys. J.* **777**, 52. DOI.

Zharkova, V.V., Aboudarham, J., Zharkov, S., Ipson, S.S., Benkhalil, A.K., Fuller, N.: 2005, Solar feature catalogues in EGSO. *Solar Phys.* **228**, 361. DOI.

Zirin, H.: 1966, *The Solar Atmosphere*, Blaisdell, Waltham.